NANO LETTERS

Letter

pubs.acs.org/NanoLett

Giant Spin Pumping and Inverse Spin Hall Effect in the Presence of Surface and Bulk Spin−Orbit Coupling of Topological Insulator Bi_2Se_3

Mahdi Jamali,[†] Joon Sue Lee,[‡] Jong Seok Jeong,[§] Farzad Mahfouzi,[∥] Yang Lv,[†] Zhengyang Zhao,[†] Branislav K. Nikolić,[⊥] K. Andre Mkhoyan,[§] Nitin Samarth,*[,‡] and Jian-Ping Wang*[,†]

[†]Department of Electrical and Computer Engineering, University of Minnesota, Minneapolis, Minnesota 55455, United States

[‡]Department of Physics, The Pennsylvania State University, University Park, Pennsylvania 16802, United States

[§]Department of Chemical Engineering and Materials Science, University of Minnesota, Minneapolis, Minnesota 55455, United States

[∥]Department of Physics, California State University, Northridge, California 91330-8268, United States

[⊥]Department of Physics and Astronomy, University of Delaware, Newark, Delaware 19716-2570, United States

Supporting Information

ABSTRACT: Three-dimensional (3D) topological insulators are known for their strong spin−orbit coupling (SOC) and the existence of spin-textured surface states that might be potentially exploited for "topological spintronics." Here, we use spin pumping and the inverse spin Hall effect to demonstrate successful spin injection at room temperature from a metallic ferromagnet (CoFeB) into the prototypical 3D topological insulator Bi_2Se_3. The spin pumping process, driven by the magnetization dynamics of the metallic ferromagnet, introduces a spin current into the topological insulator layer, resulting in a broadening of the ferromagnetic resonance (FMR) line width. Theoretical modeling of spin pumping through the surface of Bi_2Se_3, as well as of the measured angular dependence of spin-charge conversion signal, suggests that pumped spin current is first greatly enhanced by the surface SOC and then converted into a dc-voltage signal primarily by the inverse spin Hall effect due to SOC of the bulk of Bi_2Se_3. We find that the FMR line width broadens significantly (more than a factor of 5) and we deduce a spin Hall angle as large as 0.43 in the Bi_2Se_3 layer.

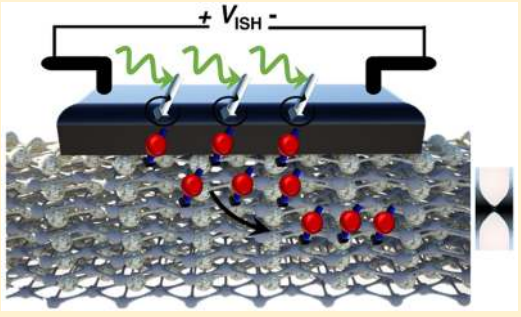

KEYWORDS: *Topological−insulator/ferromagnet heterostructures, spin pumping, spin Hall effect, interfacial spin−orbit coupling, interface intermixing, TEM, ferromagnetic resonance, spintronics*

Over the past three decades, the field of spintronics has witnessed remarkable progress on both fundamental and technological fronts. Giant magnetoresistance[1,2] and tunneling magnetoresistance[3,4] already provide the basis for a mature magnetic storage technology. Emerging device concepts now combine these phenomena with spin torque and domain wall control for applications in memory,[5,6] logic,[7,8] and sensing.[9,10] Among the many challenges that impede further progress toward applications, two issues dominate. First, the efficiency of conventional spin torque in ferromagnetic multilayers is not large enough for widespread applications, which has recently turned attention to torques generated induced by spin−orbit coupling (SOC) in heavy-metals. Second, all the successful spintronic device applications so far have been based on metallic conduction channels: the promise of semiconductor spintronics[11] that seamlessly integrates ferromagnetism with semiconductor devices remains at a developing stage. Thus, it is crucial to carry out fundamental studies of spintronic device configurations that have potential to generate large spin torque that might be readily integrated with semiconductors.

Three-dimensional topological insulators (3D TIs)[12,13] such as Bi_2Se_3 play a natural and important role in this context: they are narrow band gap semiconductors with a very strong SOC that yields helical spin-textured Dirac surface states. This spin-texture, which has been directly measured using both photoemission[14] and electrical transport,[15,16] naturally lends itself to potential exploitation for "topological spintronics." For example, several theoretical proposals have considered the possibility of manipulating the magnetization in a ferromagnetic layer via these spin-textured surface states.[17−22] Recent experiments studying spin torque ferromagnetic resonance (ST-FMR), spin-dependent tunneling and dc current-driven switching have indeed demonstrated that TIs are characterized by charge-to-spin conversion efficiency which is an order of magnitude larger than that generated by heavy-metals at room temperature (in Bi_2Se_3)[23,24] and up to 2 orders of magnitude larger at liquid helium temperature (in $(Bi,Sb)_2Te_3$).[25] In the absence of bulk charge carriers, one of the key mechanisms[22] behind spin torque is current-driven nonequilibrium spin density due to spin-momentum locking on the surface of TI, which is a substantially enhanced[26,27] variant of the so-called

Received: August 15, 2015
Published: September 14, 2015

DOI: 10.1021/acs.nanolett.5b03274
Nano Lett. 2015, 15, 7126−7132

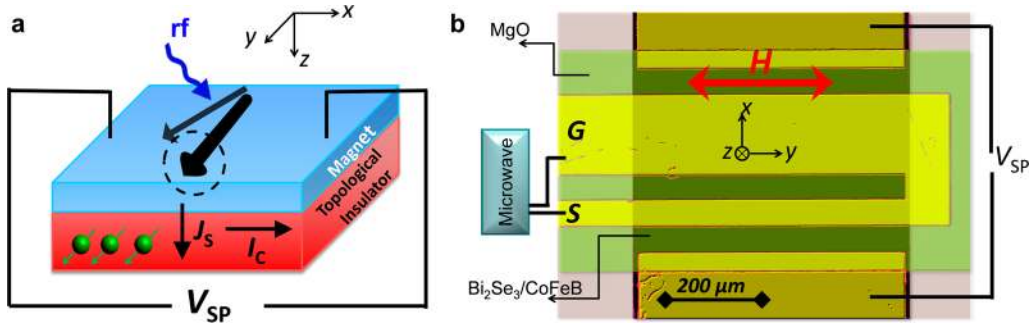

Figure 1. (a) Schematic of the device utilized for the spin pumping experiment. A thin magnetic layer is placed on the top of TI. An external rf-magnetic field, excites the magnetization dynamics. Precessional magnetization dynamics injects a net spin current (J_s) into the adjacent TI layer. Because of the strong SOC of the TI layer, this spin current is translated into a charge current that can be characterized as the output spin pumping voltage. (b) An optical micrograph of the actual fabricated device. The magnetization dynamics is excited using an asymmetric coplanar waveguide in the GS form and a microwave source.

Edelstein[28] effect originally predicted for two-dimensional electron gases with the Rashba SOC.

Other experiments[29−31] have used spin pumping to probe spin injection into TIs and the subsequent spin transport with one study attributing the observed dc-voltage signals to the inverse Edelstein effect (IEE)[32−34] on the surface of TIs.[29] In spin pumping experiments, spin current is injected from a ferromagnetic layer into a TI due to the precessional magnetization dynamics.[35−37] We note that the spin pumping process is not limited by impedance-mismatch between the magnetic and nonmagnetic layers.[38,39] The spin pumping process provides a means of probing and quantifying several important properties of the magnetic and nonmagnetic layers, such as the interfacial spin-mixing conductance and the spin Hall angle.[40]

However, there are fundamentally important questions unanswered by these experiments: do the large spin torques and spin-charge conversion signals measured in the topological−insulator/ferromagnet heterostructures actually arise from the spin-textured surface states or could they simply be generated by the bulk states that also have a large SOC? Moreover, the effect of strong SOC[41,42] present directly at the ferromagnet/nonmagnet interface, which is introduced by the surface of TI, has been absent from the standard analysis of spin pumping experiments.[43−47] These questions are particularly germane in room-temperature experiments that involve TI films where the chemical potential lies in the bulk bands.

In this paper, we seek to address these questions through a careful spin pumping study. We find that in a spin pumping geometry it is very difficult to distinguish the dc-voltage signal generated by IEE on the TI surface states from the dc-voltage signal generated by the inverse spin Hall effect (ISHE) in the bulk of TI, unless the dependence on the precession cone angle is properly characterized. We also examine the sensitivity of the spin injection efficiency to interface disorder using high-resolution transmission electron microscopy (HRTEM) and compositional mapping, showing how this can be affected by heat treatment. With proper sample preparation, we show that a spin Hall angle as large as 0.43 can be achieved in the bulk of Bi_2Se_3.

Our experiments are carried out on Bi_2Se_3/CoFeB bilayers. Electrical and optical measurements report that the bulk of Bi_2Se_3 is a semiconductor with a moderately large band gap of about 0.35 eV.[32−35] Depending on the Bi_2Se_3 sample preparation conditions, the charge transport properties can vary significantly with a tendency toward an n-type extrinsic semiconductor behavior due to the presence of vacancies or dislocations and also because of excessive selenium.[48,49] Bi_2Se_3 thin films are synthesized on semi-insulating InP(111)A substrates by molecular beam epitaxy (MBE) in ultrahigh-vacuum (UHV) systems (low 10^{-10} Torr). After desorbing native oxide on the InP(111)A substrate under As flux, the substrate is transferred to another UHV chamber without breaking vacuum for Bi_2Se_3 growth. At a substrate thermocouple temperature of 315−350 °C, single crystalline Bi_2Se_3 films are grown using thermal evaporation of high-purity (99.999%) elemental Bi and Se via conventional Knudsen cells with a Se/Bi beam equivalent pressure ratio of ∼15:1 and a growth rate ranging from ∼0.36 nm/min to ∼0.83 nm/min. The morphology of the surface is monitored by reflection high-energy electron diffraction (RHEED) during the film growth [see Supporting Information Figure S1]. Next, the substrate is cooled down to ambient temperature under the Se flux for minimizing defects such as Se vacancies. Moreover, Se serves as the capping layer for transferring the sample from MBE into the sputtering system. For comparison, samples without Se capping layer are also prepared which are protected from oxidation by photoresist (PR).

The surface of the Bi_2Se_3 thin film typically shows 1 nm steps of quintuple layers (QLs) where each QL consists of five atomic layers of Se−Bi−Se−Bi−Se [see Supporting Information Figures S1and S2]. The temperature dependence of the resistivity of the Bi_2Se_3 samples shows metallic behavior, characteristic of a degenerately doped semiconductor with significant bulk conduction at room temperature. Hall measurements of the patterned Bi_2Se_3 films [Supporting Information Figure S3] reveal a 2D carrier density of a 10 QL film of about 2.5×10^{13} cm^{-2}, indicating that the chemical potential is above the bottom of the bulk conduction band.

We investigate the spin dynamics at the Bi_2Se_3/CoFeB interface using spin pumping. The sample geometry is shown in Figure 1a. An ultrahigh vacuum (UHV) six-target Shamrock sputtering system with an in situ ion-milling source has been used for the ferromagnetic layer deposition. On the samples with Se capping layer, Se capping is removed in an AJA sputtering system with a built-in heater. Samples are heated up to 270 ± 20 °C for an hour and then cooled down. Samples are heated up for long enough time to confirm complete removal of the capping layer. On the sample with PR protection layer, the PR is simply removed utilizing Acetone solution. Samples

DOI: 10.1021/acs.nanolett.5b03274
Nano Lett. 2015, 15, 7126−7132

are then immediately transferred to our Shamrock system for the magnetic layer deposition. The TI surface is slightly etched using an ion-miller before CoFeB deposition. $Co_{20}Fe_{60}B_{20}$ (5 nm) has been deposited for the magnetic layer and the film is capped with MgO (2 nm) to prevent the magnetic layer oxidation. For the spin pumping devices, photolithography was used to define TI/ferromagnet regions. After coating the substrate with a negative-tone photoresist, the resist is patterned into rectangles with a size of 1500 μm × 620 μm. The patterns are transferred to the TI/ferromagnet layer using argon ion etching and subsequent resist removal. In order to isolate the ferromagnetic structure from the coplanar waveguide, MgO (50 nm) is sputtered. After patterning the coplanar waveguides and contacts, Cr (5 nm)/Cu (100 nm) is deposited by Ebeam evaporator followed by lift-off of the resist. For ST-FMR devices, after patterning of the stack structure into rectangular with a length of 30 μm and width of 3−30 μm, symmetric GSG waveguide is patterned and placed on top of the structure [see Supporting Information Figure S8]. Samples BS1 (10 QL), BS2 (10 QL), BS3 (10 QL), and BS4 (5 QL) are from four different batch of samples that are initially capped with Se. Sample BS5 (10 QL) is protected with PR. To characterize large precession cone angle, a spin pumping device BS6 (10 QL) is fabricated with a coplanar waveguide width of 12 μm for the signal line.

The magnetization dynamics are excited in the magnetic layer using a GHz-rf field. Because of the spin pumping effect, a net spin current (J_s) is injected into the Bi_2Se_3. The large SOC of TI converts this spin current into a charge current $J_c = \eta(2e/\hbar)J_s$ that can be read out as V_{SP} where η is the efficiency of spin to charge conversion. In the case of the inverse spin Hall effect, η is the same as θ_{SH}, the spin Hall angle. The actual fabricated device with the measurement setup is shown in Figure 1b. The magnetization dynamics are excited using an asymmetric coplanar waveguide in the GS form utilizing a microwave sinusoidal source. The width of the signal (S) and ground (G) lines are 60 and 180 μm respectively and spacing between them is 60 μm. The coplanar waveguide is isolated from the magnetic and TI layers by a 50 nm thick MgO layer. For the magnetic layer, CoFeB (5 nm) is sputtered deposited on the Bi_2Se_3 film using a Shamrock sputtering system. The surface of the Bi_2Se_3 layer is slightly etched using an in situ argon ion miller to provide a fresh interface for the magnetic layer. Using subsequent optical lithography process, the Bi_2Se_3 layer is patterned into a rectangular shape of 1.5 mm × 0.62 mm. In this report, we present experimental results for five samples BS1 (10 QL), BS2 (10 QL), BS3 (10 QL), BS4 (5 QL), and BS5 (10 QL).

Figure 2a shows the output dc-voltage for an excitation frequency of 4 GHz and an excitation amplitude of 2.5 V in sample BS1(10 QL). The output signal polarity alters as the direction of the magnetic field reverses while the absolute value of the resonance field remains the same value of 10 mT, which is consistent with typical spin pumping spectra.[35] In addition, by increasing the input excitation frequency to 6 and 8 GHz (Figure 2b,c), the resonance field shifts to 21.2 and 36.7 mT, respectively [see Supporting Information Figure S4 for contour plot]. These results are consistent with an FMR spectrum governed by the Kittel formula $f = (\gamma/(2\pi))(H(H + M_s))^{1/2}$ where M_s is the saturation field of the CoFeB and γ is the gyromagnetic ratio.[35] The spin pumping signal has the form of a symmetric Lorentzian function. Usually there are contributions from the anisotropic magnetoresistance (AMR) and/or

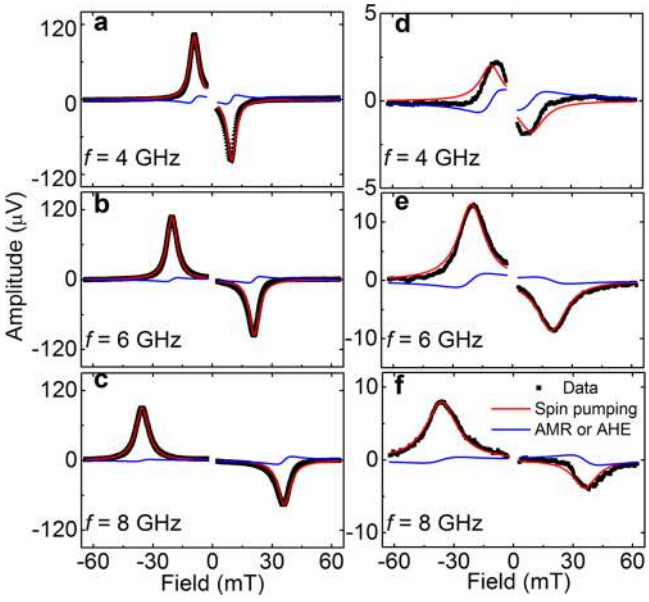

Figure 2. Spin pumping measured for the sample BS1. The output dc-voltage measured at excitation frequencies of (a) 4, (b) 6, and (c) 8 GHz for various bias fields. The experiment data (black) is overlaid with the symmetric Lorentzian (red) and antisymmetric Lorentzian (blue) curve fitting. Right column shows the spin pumping signal for the sample BS2 measured at the excitation frequency of (d) 4, (e) 6, and (f) 8 GHz. The experiment data (black) is overlaid with the symmetric Lorentzian (red) and antisymmetric Lorentzian (blue) curve fitting.

the anomalous Hall effect (AHE) of the magnetic layer (CoFeB) in the output voltage. Both AMR and AHE have the form of asymmetric Lorentzian functions and can be isolated from the output signal. By fitting the experimental spectra to the form $V = V_{SP}((\Delta H^2)/(\Delta H^2 + (H - H_r)^2)) + V_{Asym}((\Delta H(H - H_r))/(\Delta H^2 + (H - H_r)^2))$, the symmetric and asymmetric components are extracted [see Figure 2a−c]. Here, H_r is the resonant field and ΔH is the line width of the spin pumping signal.

In Figure 2d−f, the spin pumping spectra are given for the sample BS2 (10 QL) [see Supporting Information Figure S5 for the contour plot]. The results show that the line width of the spin pumping signal more than doubles compared to the sample BS1. The line width of the sample BS1 are 5.4, 6.2, and 7.7 mT, while the ones for the sample BS2 are 15.3, 17.3, 18.2 mT for the excitation frequencies of 4, 6, and 8 GHz, respectively. Further, the amplitude of the output voltage drops by more than an order of magnitude in sample BS2. The asymmetric component of the output signal is dissociated from the output signal as presented in Figure 2d−f. Because the spin pumping line width is associated with the nature of the damping of magnetization at the Bi_2Se_3/CoFeB interface, we conclude that the interfaces behave differently in samples BS1 and BS2.

In Figure 3a,b, the spin pumping spectra are given for excitation amplitudes of 1.0, 1.5, 2.0, and 2.5 V for sample BS1 and BS2, respectively. The amplitude of the spin pumping increases with excitation amplitude for both positive and negative fields. Further, the broadening of the output signal for BS2 is larger than BS1 for all excitation amplitudes. In Figure 3c,d, the amplitude of the output signal peak position is shown for different microwave excitation amplitudes. In both samples BS1 and BS2, the output amplitude increases quadratically

DOI: 10.1021/acs.nanolett.5b03274
Nano Lett. 2015, 15, 7126−7132

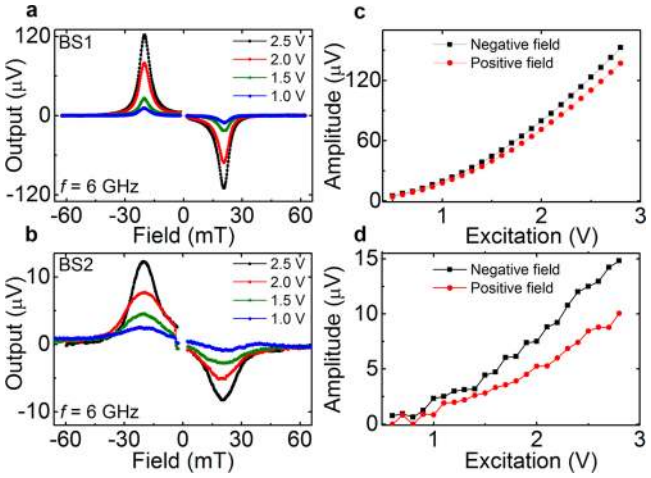

Figure 3. Spin pumping output signal for the excitation amplitude of 2.5, 2.0, 1.5, and 1.0 V for the sample BS1 at the excitation frequency of 6 GHz (a) and for the sample BS2 at the excitation frequency of 6 GHz (b). The peak amplitude of the spin pumping signal at different excitation amplitude for the sample BS1 at the excitation frequency of 6 GHz (c) and for the sample BS2 at the excitation frequency of 6 GHz (d).

relative to the input amplitude, again consistent with the spin pumping properties.[35,50]

In Figure 4a, the spin-pumping spectra are shown for samples BS1−BS5 at a constant excitation frequency of 6 GHz and for an excitation amplitude of 2.5 V. The data clearly show a wide variation of the output signal amplitude among these five samples. The amplitudes are 122, 13.2, 68, 1.5, and 71 μV for BS1−BS5, respectively. The change of the resonance field is due to slight variations of the saturation magnetization of the

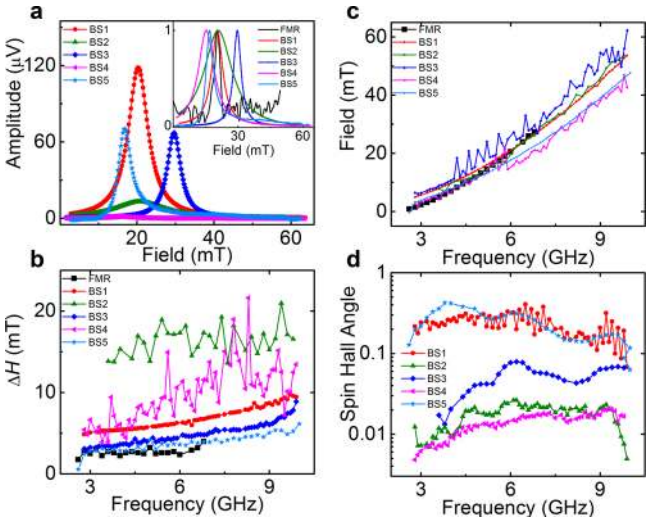

Figure 4. (a) The spin pumping spectra for the sample BS1 (10 QL), BS2 (10 QL), BS3 (10 QL), BS4 (5 QL), and BS5 (10 QL). The microwave excitation frequency is 6 GHz and the input excitation amplitude is 2.5 V for all the measurements. In the inset the normalized spin pumping signals for the samples BS1, BS2, BS3, BS4, and BS5 are given together with the FMR spectra. (b) The line width of the FMR and of the spin pumping signals of the samples BS1, BS2, BS3, BS4, and BS5. (c) The resonance fields for different excitation frequencies for the FMR and for the samples BS1, BS2, BS3, BS4, and BS5. (d) Spin Hall angles are extracted for BS1−BS4 at different excitation frequencies.

five samples. In the inset of Figure 4a, the normalized spin pumping signals are plotted versus the FMR signal. The FMR signal itself is extracted from an independent measurement of a reference CoFeB sample deposited on Si/Si_2O_3. The line width of the spin pumping signal is always larger than the FMR signal in all five samples. Moreover, BS2 has the largest value of 17.3 mT and BS5 has the smallest value of 4.1 mT while the FMR line width is 2.3 mT. Figure 4b shows the line width of samples BS1−BS5 overlaid with the FMR signal line width under different excitation frequencies. As expected, all the BS1−BS5 devices have a line width that is much larger than the FMR signal. Moreover, there is a wide variation of the line width among these five samples.

The pumped spin current flows mostly[33] into the surface of TI when its bulk is highly resistive, where it is converted into a charge current, or a dc-voltage in an open circuit, by SOC on the surface of TI via IEE. If the bulk of the TI layer has sufficiently low resistivity, pumped spin current is injected into the bulk and converted to a dc-voltage via the ISHE of the bulk. Both dc-voltage signals appear in the same direction as $\vec{J}_s \times \hat{\sigma}$ and they are picked up by the same dc-probe configuration placed on the top of Bi_2Se_3/CoFeB heterostructure in Figure 1a.

To understand the origin of the dc-voltage signal, we extracted the magnetization precession cone angle for different excitation amplitude at a fixed frequency of 6 GHz [see Supporting Information Figure S13]. In all samples, we find that the spin pumping output signal is proportional to $\sin^2\theta$. Using a charge conserving Floquet-nonequilibrium Green function (Floquet-NEGF) formalism,[41] we calculate the angular dependence of V_{pump}^{IEE},[34] as well as of spin current $I_{pump}^{S_y}$ injected by pumping into the bulk of the Bi_2Se_3 [see Supporting Information for more information]. The angular dependence of V_{pump}^{ISHE} is proportional to I^{S_y} and is thus identical to that of I^{S_y}, while its magnitude depends on bulk material specific parameters.[40] The distinction between the two dependences is conspicuous even at small cone angles $\theta \leq 30°$. Interestingly, the V_{pump}^{ISHE} versus θ dependence is identical to the one generated in conventional F/N (N-normal metal) bilayers without interfacial SOC,[43] which is also consistent with other very recent theoretical studies.[42] Because our experimental data has the same $\sin^2\theta$ dependence, this confirms that we have injected pure spin current into the bulk of the TI layer at room temperature.

Having established that the ISHE is likely dominant over the IEE, we estimated θ_{SH} using the formula derived for a conventional ferromagnetic metal/normal metal bilayer. The broadening of the spin pumping line width is closely related to the spin mixing conductance at the interface of Bi_2Se_3/CoFeB. The spin mixing conductance is evaluated from the relation $g^{\uparrow\downarrow} = ((2\sqrt{3}\pi M_s \gamma d_{CFB})/(g\mu_B\omega))(\Delta H_{SP} - \Delta H_{FMR})$, where d_{CFB} is the thickness of the CoFeB, ω (= $2\pi f$) the excitation frequency, μ_B is the Bohr magneton, and g is the Landau g-factor. In Figure 4c, the resonant field is given for different excitation frequencies of spin pumping in samples BS1−BS5 and for FMR. All the samples show the same behavior with a slight difference in the resonance field. By fitting the data to the Kittel formula, the saturation magnetization is extracted independently [see Supporting Information Figure S6]. The spin mixing conductance is found to be 6.5×10^{19}, 26×10^{19}, 2.9×10^{19}, 14×10^{19}, and 1.2×10^{19} m^{-2} for BS1−BS5, respectively, at the excitation frequency of 6 GHz. The wide variation of spin pumping line width and spin mixing conductance could also be

DOI: 10.1021/acs.nanolett.5b03274
Nano Lett. 2015, 15, 7126−7132

understood based on the Rashba SOC of the surface state. From our simulation results, we find that pumped spin current into the bulk of TI can be enhanced by the interfacial SOC [see Supporting Information Figure S14b and its discussion]. Therefore, depending on the strength of SOC of the surface state, the injected spin current into the bulk of Bi_2Se_3 could be amplified, resulting in the broadening of the FMR line width and a larger spin mixing conductance.

Knowing the spin mixing conductance, the spin current density injected from the ferromagnet into the Bi_2Se_3 layer can be calculated from $j_s = ((g^{\uparrow\downarrow}\gamma^2 h_{rf}^2 \hbar[M_s\gamma + ((M_s\gamma)^2 + 4\omega^2)^{1/2}])/(8\pi\alpha^2[(M_s\gamma)^2 + 4\omega^2]))$[51] where h_{rf} is the excitation rf-field and α is the Gilbert damping coefficient. The damping coefficient can be calculated from $\alpha = ((\sqrt{3}\gamma\Delta H)/2\omega)$.[35,52] In order to evaluate the spin current density, we need to estimate the rf-field carefully. We use a vector network analyzer to characterize the input impedance at different excitation frequencies and calculate the h_{rf}, accordingly [see Supporting Information Figure S7]. The spin current density given by $(2e/\hbar)j_s$ is about 1×10^7, 3.3×10^6, 1.0×10^7, 2.6×10^6, and 2.8×10^6 A/m^2 for samples BS1−BS5 at the excitation frequency of 6 GHz.

The output voltage can be related to the spin current and the spin Hall angle according to the formula $V_{ISHE} = ((w\theta_{SHE}\lambda_N \tanh(d_N/2\lambda_N))/(d_N\sigma_N + d_F\sigma_F))(2e/\hbar)j_s$,[51] where d_N is the thickness of the Bi_2Se_3 and λ_N is the spin coherence length of the TI channel. In Figure 4d, we calculate θ_{SH} for different resonance frequencies in sample BS1−BS5 [see Supporting Information Figure S8 for details]. At the excitation frequency of 6 GHz, θ_{SH} = 0.33, 0.026, 0.08, 0.015, and 0.34 for samples BS1−BS5, respectively. It is clear that the value of θ_{SH} can vary by more than an order of magnitude from sample to sample. Our calculated value of θ_{SH} for sample BS5 is about 2 orders of magnitude larger than of the recent report on the spin pumping into TI.[30] Moreover, the extracted θ_{SH} of sample BS1 is consistent with the large spin torque angle[23] and spin Hall angle[24] measured recently in Bi_2Se_3. Because the current density involved during our measurement is very small, our results are free from spurious effects like Joule heating. From Figure 4d, we see a weak dependence of θ_{SH} on the excitation microwave frequency. Over an excitation frequency range of 3 to 9 GHz, θ_{SH} has maximum value of 0.41, 0.028, 0.083, 0.021, 0.43 in samples BS1−BS5, respectively.

The wide fluctuation of spin pumping signals from sample to sample could be explained based on the nonuniform composition of Bi_2Se_3 at its interface with the magnetic layer. Recently, it has been shown that surfaces of TIs are very nonuniform in terms of chemical potential and position of Dirac point.[53] Because the Bi_2Se_3/CoFeB interface plays the major role in the spin injection, the large variations of the spin pumping characteristics could be associated with nonuniform Bi_2Se_3 surface. Moreover, the decapping process could also be responsible for modification of the TI surface considering Bi_2Se_3 has strong thermoelectric properties.[54] Comparing the samples BS1−4 with BS5, BS5 is not involved in any high-temperature decapping process and we obtain the maximum spin Hall angle in this sample. This suggests that heat treatment of TI samples could modify the surface state of TI due to change of the material composition at the surface. In addition, surface roughness can modify the spin pumping efficiency.[55] As discussed before, the surface of Bi_2Se_3 is not very smooth and potentially it can alter the spin pumping signal.

To better understand the interface between the Bi_2Se_3 and CoFeB, we performed annular dark-field scanning transmission electron microscopy (ADF-STEM) imaging and energy dispersive X-ray spectroscopy (EDX) elemental mapping using an aberration-corrected FEI Titan G2 60-300 STEM equipped with a Super-X EDX spectrometer on cross-sectional Bi_2Se_3/CoFeB thin film samples. Electron-transparent STEM specimens were prepared using a focused ion beam (FIB) lift-out (FEI Quanta 200 3D). FIB specimen preparation was conducted using a 30 keV Ga-ion beam followed by a 5 keV Ga-ion beam to minimize Ga-ion-damaged layers. An aberration-corrected FEI Titan G2 60-300 STEM equipped with a CEOS DCOR probe corrector and Super-X EDX spectrometer is used in this study. ADF-STEM imaging and EDX mapping are done on the microscope operated at 300 keV with the collection angle for ADF detector 50−300 mrad and the convergent semiangle of the incident STEM probe 24.5 mrad. Beam currents of ∼50 and ∼150 pA are used for ADF-STEM imaging and EDX mapping. It is confirmed that no detectable beam damage has occurred under these conditions.

The resulting ADF-STEM image is shown in Figure 5a. Starting from the InP substrate with (111) surface, Bi_2Se_3 layer

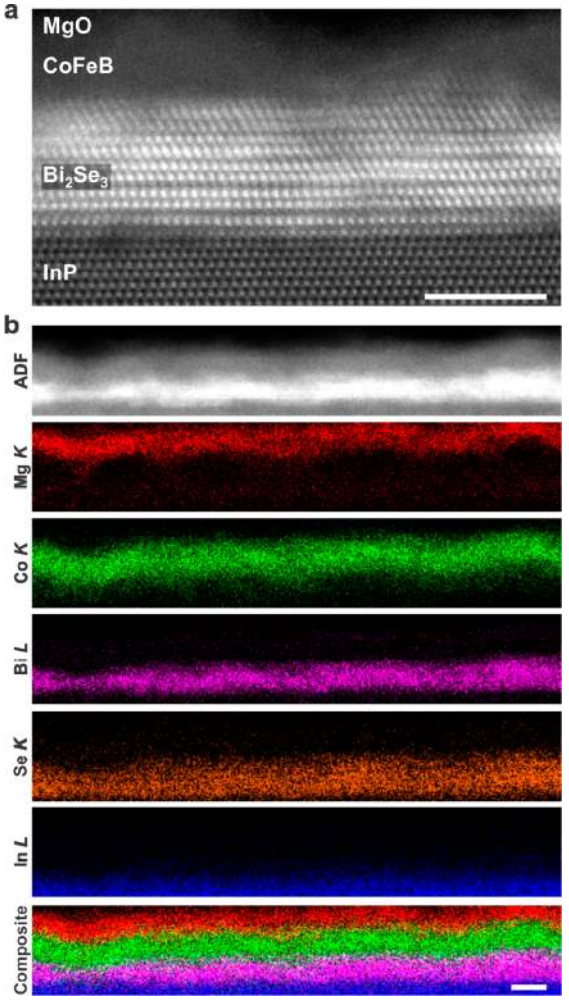

Figure 5. (a) Cross-sectional high-resolution ADF-STEM image of a TI/CoFeB/MgO sample. (b) EDX elemental maps of Mg K, Co K, Bi L, Se K, and In L signals form the sample. All EDX maps and ADF-STEM image in (b) are acquired simultaneously. The composite map is produced by combining Mg, Co, Bi, and In X-ray signals. The ADF-STEM image and the EDX maps reveal that the films have surface roughness over lateral distance. The scale bars are 5 nm.

DOI: 10.1021/acs.nanolett.5b03274
Nano Lett. 2015, 15, 7126−7132

forms a crystalline structure with quite a rough surface. In the Bi_2Se_3 layer, two bright atomic layers separated by dark strips corresponds to each QL. CoFeB is amorphous and is partially diffused into the Bi_2Se_3 layer at some locations. The diffusion of atoms from CoFeB into the Bi_2Se_3 is no surprise because this is a very soft material and the sputtering process is very energetic (see Supporting Information for STEM images). The EDX elemental maps are presented in Figure 5b for Mg, Co, Bi, Se, and In elements [see Supporting Information for full elemental analysis]. The EDX results suggest that the lateral distribution of Se is wider compared to Bi, an effect that could be a result of Bi_2Se_3 heat treatment during the decapping process.

As a comparison to the recent ST-FMR characterization of θ_{SH}, we also perform ST-FMR measurements and compare the results with the spin pumping [see Supporting Information Figures S9 and S10]. Our ST-FMR measurements yield θ_{SH} as high as 1.7 at low frequency, consistent with the recent report. Further, at high frequency the values of θ_{SH} from ST-FMR and from spin pumping match well with each other.

In summary, we have carried out spin pumping experiments at Bi_2Se_3/CoFeB interfaces. Our results clearly demonstrate the successful pumping of a spin current into the TI layer at room temperature and a large spin Hall angle. In highly bulk-conductive Bi_2Se_3 TIs, the inverse Hall effect of the bulk seems to dominate over the inverse Edelstein effect of the surface state, at least in spin pumping experiments. Moreover, we find that the spin pumping characteristics vary from sample to sample, likely due to a nonuniform CoFeB/Bi_2Se_3 interface and heat treatment of samples. Our experimental results confirm that 3D TIs such as Bi_2Se_3 do indeed show large value of the spin Hall angle in both ST-FMR and spin pumping experiments, but these large effects could also arise from the "trivial" bulk states. A clear understanding of the differentiation between contributions of these bulk states from those of the topological surface states will be important for the development of topological spintronics.

■ ASSOCIATED CONTENT

Supporting Information

The Supporting Information is available free of charge on the ACS Publications website at DOI: 10.1021/acs.nanolett.5b03274.

The Bi_2Se_3 thin film growth and characterizations, details of the spin pumping experiments and spin Hall angle characterizations, TEM imaging and EDX spectroscopy images, and theoretical calculation of IEE and ISHE. (PDF)

■ AUTHOR INFORMATION

Corresponding Authors

*E-mail: jpwang@umn.edu.
*E-mail: nsamarth@psu.edu.

Notes

The authors declare no competing financial interest.

■ ACKNOWLEDGMENTS

This work was partially supported by the C-SPIN center, one of six STARnet program research centers and National Science Foundation Nanoelectronics Beyond 2020 (Grant NSF NEB 1124831). B.K.N. was supported by NSF Grant No. ECCS 150909.

■ ABBREVIATIONS

TI: topological insulator; IEE: inverse Edelstein effect; ISHE: inverse spin Hall effect; FMR: ferromagnetic resonance; ST-FMR: spin torque ferromagnetic resonance; SOC: spin−orbit coupling; QL: quintuple layer

■ REFERENCES

(1) Barnaś, J.; Fuss, A.; Camley, R. E.; Grünberg, P.; Zinn, W. Novel Magnetoresistance Effect in Layered Magnetic Structures: Theory and Experiment. *Phys. Rev. B: Condens. Matter Mater. Phys.* **1990**, *42*, 8110−8120.

(2) Baibich, M. N.; Broto, J. M.; Fert, A.; Van Dau, F. N.; Petroff, F.; et al. Giant Magnetoresistance of (001)Fe/(001)Cr Magnetic Superlattices. *Phys. Rev. Lett.* **1988**, *61*, 2472−2475.

(3) Parkin, S. S. P.; Kaiser, C.; Panchula, A.; Rice, P. M.; Hughes, B.; Samant, M.; Yang, S.-H. Giant Tunnelling Magnetoresistance at Room Temperature with MgO (100) Tunnel Barriers. *Nat. Mater.* **2004**, *3*, 862−867.

(4) Ikeda, S.; Miura, K.; Yamamoto, H.; Mizunuma, K.; Gan, H. D.; Endo, M.; Kanai, S.; Hayakawa, J.; Matsukura, F.; Ohno, H. A Perpendicular-Anisotropy CoFeB-MgO Magnetic Tunnel Junction. *Nat. Mater.* **2010**, *9*, 721−724.

(5) Parkin, S. S. P.; Hayashi, M.; Thomas, L. Magnetic Domain-Wall Racetrack Memory. *Science* **2008**, *320*, 190−194.

(6) Everspin. *ST-MRAM Press Release*; 2012.

(7) Meng, H.; Wang, J.; Wang, J. P. A Spintronics Full Adder for Magnetic CPU. *IEEE Electron Device Lett.* **2005**, *26*, 360−362.

(8) Yao, X.; Harms, J.; Lyle, A.; Ebrahimi, F.; Zhang, Y.; Wang, J.-P. Magnetic Tunnel Junction-Based Spintronic Logic Units Operated by Spin Transfer Torque. *IEEE Trans. Nanotechnol.* **2012**, *11*, 120−126.

(9) Melzer, M.; Makarov, D.; Calvimontes, A.; Karnaushenko, D.; Baunack, S.; Kaltofen, R.; Mei, Y.; Schmidt, O. G. Stretchable Magnetoelectronics. *Nano Lett.* **2011**, *11*, 2522−2526.

(10) Dieny, B.; Humbert, P.; Speriosu, V.; Metin, S.; Gurney, B.; Baumgart, P.; Lefakis, H. Giant Magnetoresistance of Magnetically Soft Sandwiches: Dependence on Temperature and on Layer Thicknesses. *Phys. Rev. B: Condens. Matter Mater. Phys.* **1992**, *45*, 806−813.

(11) Awschalom, D. D.; Flatté, M. E. Challenges for Semiconductor Spintronics. *Nat. Phys.* **2007**, *3*, 153−159.

(12) Hasan, M. Z.; Kane, C. L. Colloquium: Topological Insulators. *Rev. Mod. Phys.* **2010**, *82*, 3045−3067.

(13) Qi, X.-L.; Zhang, S.-C. Topological Insulators and Superconductors. *Rev. Mod. Phys.* **2011**, *83*, 1057−1110.

(14) Hsieh, D.; Xia, Y.; Qian, D.; Wray, L.; Dil, J. H.; Meier, F.; Osterwalder, J.; Patthey, L.; Checkelsky, J. G.; Ong, N. P.; et al. A Tunable Topological Insulator in the Spin Helical Dirac Transport Regime. *Nature* **2009**, *460*, 1101−1105.

(15) Li, C. H.; van 't Erve, O. M. J.; Robinson, J. T.; Liu, Y.; Li, L.; Jonker, B. T. Electrical Detection of Charge-Current-Induced Spin Polarization due to Spin-Momentum Locking in Bi2Se3. *Nat. Nanotechnol.* **2014**, *9*, 218−224.

(16) Tang, J.; Chang, L.-T.; Kou, X.; Murata, K.; Choi, E. S.; Lang, M.; Fan, Y.; Jiang, Y.; Montazeri, M.; Jiang, W.; et al. Electrical Detection of Spin-Polarized Surface States Conduction in (Bi(0.53)-Sb(0.47))2Te3 Topological Insulator. *Nano Lett.* **2014**, *14*, 5423−5429.

(17) Yokoyama, T. Current-Induced Magnetization Reversal on the Surface of a Topological Insulator. *Phys. Rev. B: Condens. Matter Mater. Phys.* **2011**, *84*, 113407.

(18) Garate, I.; Franz, M. Inverse Spin-Galvanic Effect in the Interface between a Topological Insulator and a Ferromagnet. *Phys. Rev. Lett.* **2010**, *104*, 146802.

(19) Mahfouzi, F.; Nagaosa, N.; Nikolić, B. K. Spin-Orbit Coupling Induced Spin-Transfer Torque and Current Polarization in Topological-Insulator/Ferromagnet Vertical Heterostructures. *Phys. Rev. Lett.* **2012**, *109*, 166602.

DOI: 10.1021/acs.nanolett.5b03274
Nano Lett. 2015, 15, 7126−7132

(20) Tserkovnyak, Y.; Loss, D. Thin-Film Magnetization Dynamics on the Surface of a Topological Insulator. *Phys. Rev. Lett.* **2012**, *108*, 187201.
(21) Semenov, Y. G.; Duan, X.; Kim, K. W. Voltage-Driven Magnetic Bifurcations in Nanomagnet−topological Insulator Heterostructures. *Phys. Rev. B: Condens. Matter Mater. Phys.* **2014**, *89*, 201405.
(22) Mahfouzi, F.; Nikolić, B. K.; Kioussis, N. Large Antidamping-like Spin-Orbit Torque Driven by Spin-Flip Reflection Mechanism on the Surface of a Topological Insulator. 2015, arXiv:1506.01303.
(23) Mellnik, A. R.; Lee, J. S.; Richardella, A.; Grab, J. L.; Mintun, P. J.; Fischer, M. H.; Vaezi, A.; Manchon, A.; Kim, E.-A.; Samarth, N.; et al. Spin-Transfer Torque Generated by a Topological Insulator. *Nature* **2014**, *511*, 449−451.
(24) Liu, L.; Richardella, A.; Garate, I.; Zhu, Y.; Samarth, N.; Chen, C.-T. Spin-Polarized Tunneling Study of Spin-Momentum Locking in Topological Insulators. *Phys. Rev. B: Condens. Matter Mater. Phys.* **2015**, *91*, 235437.
(25) Fan, Y.; Upadhyaya, P.; Kou, X.; Lang, M.; Takei, S.; Wang, Z.; Tang, J.; He, L.; Chang, L.-T.; Montazeri, M.; et al. Magnetization Switching through Giant Spin-Orbit Torque in a Magnetically Doped Topological Insulator Heterostructure. *Nat. Mater.* **2014**, *13*, 699−704.
(26) Pesin, D.; MacDonald, A. H. Spintronics and Pseudospintronics in Graphene and Topological Insulators. *Nat. Mater.* **2012**, *11*, 409−416.
(27) Chang, P.-H.; Markussen, T.; Smidstrup, S.; Stokbro, K.; Nikolić, B. K. Nonequilibrium Spin Density around Surfaces of Current-Carrying Topological Insulator Thin Film: A First-Principles Quantum Transport Study. 2015, arXiv:1503.08046.
(28) Edelstein, V. M. Spin Polarization of Conduction Electrons Induced by Electric Current in Two-Dimensional Asymmetric Electron Systems. *Solid State Commun.* **1990**, *73*, 233−235.
(29) Shiomi, Y.; Nomura, K.; Kajiwara, Y.; Eto, K.; Novak, M.; Segawa, K.; Ando, Y.; Saitoh, E. Spin-Electricity Conversion Induced by Spin Injection into Topological Insulators. *Phys. Rev. Lett.* **2014**, *113*, 196601.
(30) Deorani, P.; Son, J.; Banerjee, K.; Koirala, N.; Brahlek, M.; Oh, S.; Yang, H. Observation of Inverse Spin Hall Effect in Bismuth Selenide. *Phys. Rev. B: Condens. Matter Mater. Phys.* **2014**, *90*, 094403.
(31) Baker, A. A.; Figueroa, A. I.; Collins-McIntyre, L. J.; van der Laan, G.; Hesjedal, T. Spin Pumping in Ferromagnet-Topological Insulator-Ferromagnet Heterostructures. *Sci. Rep.* **2015**, *5*, 7907.
(32) Shen, K.; Vignale, G.; Raimondi, R. Microscopic Theory of the Inverse Edelstein Effect. *Phys. Rev. Lett.* **2014**, *112*, 096601.
(33) Sánchez, J. C. R.; Vila, L.; Desfonds, G.; Gambarelli, S.; Attané, J. P.; De Teresa, J. M.; Magén, C.; Fert, A. Spin-to-Charge Conversion Using Rashba Coupling at the Interface between Non-Magnetic Materials. *Nat. Commun.* **2013**, *4*, 2944.
(34) Mahfouzi, F.; Nagaosa, N.; Nikolić, B. K. Spin-to-Charge Conversion in Lateral and Vertical Topological-Insulator/ferromagnet Heterostructures with Microwave-Driven Precessing Magnetization. *Phys. Rev. B: Condens. Matter Mater. Phys.* **2014**, *90*, 115432.
(35) Jamali, M.; Klemm, A.; Wang, J.-P. Precessional Magnetization Induced Spin Current from CoFeB into Ta. *Appl. Phys. Lett.* **2013**, *103*, 252409.
(36) Costache, M.; Sladkov, M.; Watts, S.; van der Wal, C.; van Wees, B. Electrical Detection of Spin Pumping due to the Precessing Magnetization of a Single Ferromagnet. *Phys. Rev. Lett.* **2006**, *97*, 216603.
(37) Costache, M.; Watts, S.; van der Wal, C.; van Wees, B. Electrical Detection of Spin Pumping: Dc Voltage Generated by Ferromagnetic Resonance at Ferromagnet/nonmagnet Contact. *Phys. Rev. B: Condens. Matter Mater. Phys.* **2008**, *78*, 064423.
(38) Ando, K.; Takahashi, S.; Ieda, J.; Kurebayashi, H.; Trypiniotis, T.; Barnes, C. H. W.; Maekawa, S.; Saitoh, E. Electrically Tunable Spin Injector Free from the Impedance Mismatch Problem. *Nat. Mater.* **2011**, *10*, 655−659.
(39) Ando, K.; Saitoh, E. Observation of the Inverse Spin Hall Effect in Silicon. *Nat. Commun.* **2012**, *3*, 629.
(40) Mosendz, O.; Pearson, J. E.; Fradin, F. Y.; Bauer, G. E. W.; Bader, S. D.; Hoffmann, a. Quantifying Spin Hall Angles from Spin Pumping: Experiments and Theory. *Phys. Rev. Lett.* **2010**, *104*, 046601.
(41) Mahfouzi, F.; Fabian, J.; Nagaosa, N.; Nikolić, B. K. Charge Pumping by Magnetization Dynamics in Magnetic and Semimagnetic Tunnel Junctions with Interfacial Rashba or Bulk Extrinsic Spin-Orbit Coupling. *Phys. Rev. B: Condens. Matter Mater. Phys.* **2012**, *85*, 054406.
(42) Chen, K.; Zhang, S. Spin Pumping in the Presence of Spin-Orbit Coupling. *Phys. Rev. Lett.* **2015**, *114*, 126602.
(43) Tserkovnyak, Y.; Brataas, A.; Bauer, G.; Halperin, B. Nonlocal Magnetization Dynamics in Ferromagnetic Heterostructures. *Rev. Mod. Phys.* **2005**, *77*, 1375−1421.
(44) Hyde, G. R.; Beale, H. A.; Spain, I. L.; Woollam, J. A. Electronic Properties of Bi2Se3 Crystals. *J. Phys. Chem. Solids* **1974**, *35*, 1719−1728.
(45) Zhang, H.; Liu, C.-X.; Qi, X.-L.; Dai, X.; Fang, Z.; Zhang, S.-C. Topological Insulators in Bi2Se3, Bi2Te3 and Sb2Te3 with a Single Dirac Cone on the Surface. *Nat. Phys.* **2009**, *5*, 438−442.
(46) Greanya, V. A.; Tonjes, W. C.; Liu, R.; Olson, C. G.; Chung, D.-Y.; Kanatzidis, M. G. Determination of the Valence Band Dispersions for Bi[sub 2]Se[sub 3] Using Angle Resolved Photoemission. *J. Appl. Phys.* **2002**, *92*, 6658−6661.
(47) Peng, H.; Dang, W.; Cao, J.; Chen, Y.; Wu, D.; Zheng, W.; Li, H.; Shen, Z.-X.; Liu, Z. Topological Insulator Nanostructures for near-Infrared Transparent Flexible Electrodes. *Nat. Chem.* **2012**, *4*, 281−286.
(48) Black, J.; Conwell, E. M.; Seigle, L.; Spencer, C. W. Electrical and Optical Properties of Some M2v−bN3vi−b Semiconductors. *J. Phys. Chem. Solids* **1957**, *2*, 240−251.
(49) Larson, P.; Greanya, V.; Tonjes, W.; Liu, R.; Mahanti, S.; Olson, C. Electronic Structure of Bi2 × 3 (X = S, Se, T) Compounds: Comparison of Theoretical Calculations with Photoemission Studies. *Phys. Rev. B: Condens. Matter Mater. Phys.* **2002**, *65*, 085108.
(50) Costache, M. V.; Sladkov, M.; Watts, S. M.; van der Wal, C. H.; van Wees, B. J. Electrical Detection of Spin Pumping due to the Precessing Magnetization of a Single Ferromagnet. *Phys. Rev. Lett.* **2006**, *97*, 216603.
(51) Ando, K.; Saitoh, E. Inverse Spin-Hall Effect in Palladium at Room Temperature. *J. Appl. Phys.* **2010**, *108*, 113925.
(52) Kalarickal, S. S.; Krivosik, P.; Wu, M.; Patton, C. E.; Schneider, M. L.; Kabos, P.; Silva, T. J.; Nibarger, J. P. Ferromagnetic Resonance Linewidth in Metallic Thin Films: Comparison of Measurement Methods. *J. Appl. Phys.* **2006**, *99*, 093909.
(53) Beidenkopf, H.; Roushan, P.; Seo, J.; Gorman, L.; Drozdov, I.; Hor, Y. S.; Cava, R. J.; Yazdani, A. Spatial Fluctuations of Helical Dirac Fermions on the Surface of Topological Insulators. *Nat. Phys.* **2011**, *7*, 939−943.
(54) Mishra, S. K.; Satpathy, S.; Jepsen, O. Electronic Structure and Thermoelectric Properties of Bismuth Telluride and Bismuth Selenide. *J. Phys.: Condens. Matter* **1997**, *9*, 461−470.
(55) Kitamura, Y.; Shikoh, E.; Ando, Y.; Shinjo, T.; Shiraishi, M. Vertical Spin Transport in Al with Pd/Al/Ni80Fe20 Trilayer Films at Room Temperature by Spin Pumping. *Sci. Rep.* **2013**, *3*, 1739.

DOI: 10.1021/acs.nanolett.5b03274
Nano Lett. 2015, 15, 7126−7132